| | |
|---|---|
| Title | Properties of nuclei in the inner crusts of neutron stars in the relativistic mean-field theory |
| Author(s) | Cheng, KS; Yao, CC; Dai, ZG |
| Citation | Physical Review C - Nuclear Physics, 1997, v. 55 n. 4, p. 2092-2100 |
| Issued Date | 1997 |
| URL | http://hdl.handle.net/10722/43201 |
| Rights | Creative Commons: Attribution 3.0 Hong Kong License |

# Properties of nuclei in the inner crusts of neutron stars in the relativistic mean-field theory

K. S. Cheng,[1] C. C. Yao,[1] and Z. G. Dai[2]
[1]*Department of Physics, The University of Hong Kong, Hong Kong*
[2]*Department of Astronomy, Nanjing University, Nanjing 210093, China*
(Received 30 September 1996)

We study the properties of nuclei in the inner crusts of neutron stars based on the Boguta-Bodmer nonlinear model in the relativistic mean-field theory. We carefully determine the surface diffuseness of the nuclei as the density of matter increases. The imaginary time step method is used to solve the Euler-Lagrange equation derived from the variational principle applied to the semiclassical energy density. It is shown that with increasing density, the spherical nuclei become more neutron rich and eventually merge to form a uniform liquid of neutrons, protons, and electrons. We find that the smaller the value of the incompressibility $K$, the lower the density at which the phase transition to uniform matter occurs. The relativistic extended Thomas-Fermi method is generalized to investigate nonspherical nuclei. Our results show that the spherical nucleus phase is the only equilibrium state in the inner crusts of neutron stars. [S0556-2813(97)00604-3]

PACS number(s): 21.65.+f, 21.10.Ft, 26.60.+c, 97.60.Jd

## I. INTRODUCTION

It is expected that the properties of nuclei in the inner crusts of neutron stars are very different from those of terrestrial nuclei [1]. With increasing depth in a neutron star, the density of matter increases and nuclei become increasingly neutron rich to maintain the $\beta$-stability condition. At a density of about $4.0\times10^{11}$ g cm$^{-3}$, the neutron drip region occurs, which means that the most energetic neutrons are no longer bound to nuclei and start to drip off from nuclei, forming a low-density neutron gas. At higher densities, the matter inside nuclei becomes more neutron rich and the neutron gas becomes denser. As the density of matter approaches the nuclear density $\rho_0\approx2.8\times10^{14}$ g cm$^{-3}$, the neutron-rich nuclei eventually merge to form a uniform liquid of neutrons and protons, together with a uniform background of relativistic electrons (for a general review of the crustal structure of neutron stars, see [2,3]).

Dense matter in the inner crust is composed of nuclei, neutrons, and electrons under the conditions of charge neutrality and $\beta$ stability. The temperature of the crustal matter can be assumed to be absolute zero. In the region of interest, the thermal energy $k_BT$ ($T\leqslant10^9$ K) is much less than the Fermi energies of neutrons and electrons. Therefore it is certain that the assumption of zero temperature is a valid approximation.

Since the discovery of pulsars, investigation of the matter at subnuclear densities has become a growing interest. The earliest important works were done by Langer *et al.* [4] and Bethe, Börner, and Sato [5]. Both of them treated the free neutron regime based on extrapolations from the semiempirical mass formula. However, because of the fact that the mass formula's parameters were determined by the very restricted region of nuclear configurations which are very different from that in the free neutron regime, it is obvious that extrapolations based on the semiempirical mass formula were unreliable. An improvement was made by Baym, Bethe, and Pethick [6], who considered the reduction of surface energy in nuclear matter caused by outside neutron gas and calculated the energy of nuclear matter in nuclei and that of neutron matter outside from the same expression as a function of neutron and proton densities. Similar calculations were done by Arponen [7] and Buchler and Barkat [8]. They both determined the ground-state density distributions variationally in a Thomas-Fermi theory, and by introducing a gradient term in the expression for the energy, the surface energy was included in their calculations. The most detailed study was carried out by Negele and Vautherin [1], who used Hartree-Fock calculations to investigate the ground-state configuration of neutron-star matter at subnuclear density.

It was first proposed by Ravenhall *et al.* [9] that unusual nuclear shapes are favored at certain densities and the nuclear shapes change from sphere to cylinder, slab, cylindrical hole, and spherical hole successively with increasing density. They described the system in terms of the compressible liquid drop model and treated the dimensionality of nuclear shapes as a continuous variable. They pointed out that as the density increases, the volume fraction of nuclei increases and the relative surface area can be reduced by changing nuclear shapes. Consequently, the surface energy and the Coulomb energy can be reduced. Derived from a purely geometrical argument, similar results were obtained in [10,11], where the compressible liquid drop model was also used and a sharp nuclear surface was assumed. Recently, Oyamastsu [12], who used the Thomas-Fermi calculations in the zero-temperature approximation, refined the previous calculations by considering both the surface diffuseness and several nuclear shapes and lattice types with parametrized neutron and proton distributions. His study also confirmed the liquid drop results of existing nonspherical nuclei in the inner crust of neutron stars. It was pointed out that the presence of nonspherical nuclei could affect significantly pinning of vortices and neutrino emission inside neutron stars [13]. Recently, it was shown that a sizable increase in the specific heat is expected if nonspherical nuclei exist [14].

However, the existence of nonspherical nuclei in the inner crust of neutron stars is still uncertain and further detailed investigations are required. This is because one requires to estimate the energy of an interface between nuclear matter

 

and neutron matter with extremely good accuracy. Besides, the obtained configurations of nucleons must be in the ground state and satisfy the equilibrium conditions. Generally, in order to make the calculation as simple as possible, it is always using approximations to estimate the Coulomb and surface energy of the nuclear system. In addition, the energy differences between various shapes of nuclei and uniform matter are extremely small compared with the bulk energy of the uniform matter. The binding energy differences among various nuclear shapes are of order of ~1 keV, but the typical bulk energy of uniform matter is ~1 MeV [12].

The purpose of this paper is to study properties of the nuclei in the inner crust of neutron stars by using recently developed nuclear theories and careful numerical calculations. In the present work we use the relativistic extended Thomas-Fermi (RETF) calculations for the nonlinear ($\sigma,\omega,\rho$) model in the relativistic mean-field theory (RMFT). During recent years, the relativistic many-body approach to nuclear systems has been of growing interest. It is known that the simplest way to describe nuclear matter which is consistent with relativity and the known bulk properties of nuclear matter is using the relativistic mean-field (RMF) theory (see [15]). In the standard model of Walecka [16] the incompressibility $K$ of nuclear matter is overestimated. To solve this problem, Boguta and Bodmer [17] (BB) added cubic and quartic terms to the scalar field. We will apply the nonlinear BB ($\sigma,\omega,\rho$) model to describe the nuclear system. Besides, in order to avoid the difficulty of a wave function treatment, we will use the semiclassical relativistic extended Thomas-Fermi approximation proposed by Centelles *et al.* [18,19] instead of using the complicated Hartree approximation.

The global properties of a neutron star such as mass, radius, and moment of inertia have been studied by the present authors elsewhere [20]. We will first consider spherical nuclei and uniform matter. In uniform matter, the nuclear surface and curvature as well as Coulomb effects are ignored. The particle and energy densities of the system are derived from the semiclassical relativistic extended Thomas-Fermi calculations up to second order in $\hbar$, based on the effective Lagrangian density of the nonlinear BB model. Then we will generalize the method to nonspherical nuclei and determine the possibility of nonspherical nuclei.

This paper is organized as follows. In Sec. II, we present the effective Lagrangian density and derive the energy densities. The choice of parameter scheme is discussed in Sec. III. In Sec. IV, we describe the numerical scheme. The results of the energies of spherical nuclei and uniform matter, as well as nucleon density distributions, are presented in Sec. V, where the results for nonspherical nuclei are presented. A brief discussion and conclusions are given in Sec. VI.

## II. EFFECTIVE LAGRANGIAN DENSITY AND ENERGY DENSITIES

We start from the effective Lagrangian density which treats nucleons as Dirac spinors $\psi$ interacting through the exchange of several mesons between nucleons through the Yukawa coupling. We here use the model which includes nucleons, scalar mesons $\sigma$, with nonlinear couplings, vector mesons $\omega$, isovector mesons $\rho$, and photons. The notation closely followed that of Centelles *et al.* [18,19]. The effective Lagrangian density of the nuclear system is given by ($\hbar=c=1$)

$$\begin{aligned}\mathcal{L}=&\overline{\psi[}\,\gamma_\mu(i\partial^\mu-g_v V^\mu)-m^*]\psi+\tfrac{1}{2}(\partial_\mu\phi\partial^\mu\phi-m_s^2\phi^2)\\&-\tfrac{1}{3}b\phi_0^3-\tfrac{1}{4}c\phi_0^4-\tfrac{1}{4}F_{\mu\nu}F^{\mu\nu}+\tfrac{1}{2}m_v^2V_\mu V^\mu-\tfrac{1}{4}H_{\mu\nu}H^{\mu\nu}\\&-e\overline{\psi}\gamma_\mu\tfrac{1}{2}(1+\tau_3)A^\mu\psi-\tfrac{1}{4}\mathbf{G}_{\mu\nu}\cdot\mathbf{G}^{\mu\nu}+\tfrac{1}{2}m_\rho^2\mathbf{b}_\mu\cdot\mathbf{b}^\mu\\&-\tfrac{1}{2}g_\rho\overline{\psi}\gamma_\mu\tau\cdot\mathbf{b}^\mu\psi,\end{aligned}\tag{1}$$

where

$$F_{\mu\nu}=\partial_\mu V_\nu-\partial_\nu V_\mu,\tag{2}$$

$$H_{\mu\nu}=\partial_\mu A_\nu-\partial_\nu A_\mu,\tag{3}$$

$$\mathbf{G}_{\mu\nu}=\partial_\mu\mathbf{b}_\nu-\partial_\nu\mathbf{b}_\mu.\tag{4}$$

Here $\psi$, $\phi$, $V^\mu$, and $\mathbf{b}^\mu$ denote the fields of the nucleon, the attractive isoscalar-scalar ($\sigma$) meson, the repulsive isoscalar-vector ($\omega$) meson, and the isovector-vector ($\rho$) meson with masses of $m_\sigma$, $m_\omega$, and $m_\rho$, respectively. $A^\mu$ is the electromagnetic field. The constants $g_\sigma$, $g_\omega$, and $g_\rho$ are coupling constants for interactions between mesons and nucleons. The $m^*$ is the effective nucleon mass. In the BB model,

$$m^*=m-g_s\phi.\tag{5}$$

Within the semiclassical relativistic extended Thomas-Fermi $\hbar^2$ method [18,19], the semiclassical energy density of the Lagrangian density for the neutron-star matter including the relativistic electrons is written as

$$\begin{aligned}e^{\mathrm{sc}}=&e_{\mathrm{ke}}+e_0+e_2+g_vV_0\rho+eA_0(\rho_p-\rho_e)\\&+\tfrac{1}{2}[(\nabla\phi_0)^2+m_s^2\phi_0^2]-\tfrac{1}{2}[(\nabla V_0)^2+m_v^2V_0^2]-\tfrac{1}{2}(\nabla A_0)^2\\&-\tfrac{1}{2}[(\nabla b_0)^2+m_\rho^2b_0^2]+\tfrac{1}{2}g_\rho b_0(\rho_p-\rho_n)+\tfrac{1}{3}b\phi_0^3+\tfrac{1}{4}c\phi_0^4,\end{aligned}\tag{6}$$

where

$$e_0=\sum_q\ \frac{1}{8\pi^2}\left(k_F\epsilon_F^3+k_F^3\epsilon_F-m^{*4}\ln\frac{k_F+\epsilon_F}{m^*}\right)\Bigg|_q,\tag{7}$$

$$e_2=\sum_q\ [X_{1q}(\nabla\rho_q)^2+X_{2q}(\nabla\rho_q\cdot\nabla m^*)+X_{3q}(\nabla m^*)^2],\tag{8}$$

$$X_{1q}=\frac{\pi^2}{24k_F^3\epsilon_F^2}\left(\epsilon_F+2k_F\ln\frac{k_F+\epsilon_F}{m^*}\right)\Bigg|_q, \tag{9}$$

$$X_{2q}=\frac{m^*}{6k_F\epsilon_F^2}\ln\frac{k_F+\epsilon_F}{m^*}\Bigg|_q, \tag{10}$$

$$X_{3q}=\frac{k_F^2}{24\pi^2\epsilon_F^2}\left[\frac{\epsilon_F}{k_F}-\left(2+\frac{\epsilon_F^2}{k_F^2}\right)\ln\frac{k_F+\epsilon_F}{m^*}\right]\Bigg|_q, \tag{11}$$

and

$$e_{\rm ke}=\frac{m_e^4}{8\pi^2}\{x_e(2x_e^2+1)(x_e^2+1)^{1/2}-\ln[x_e+(x_e^2+1)^{1/2}]\}, \tag{12}$$

$$x_e=\frac{(3\pi^2\rho_e)^{1/3}}{m_e}. \tag{13}$$

Here $q$ denotes the charge state of each nucleon, $\rho=\rho_p+\rho_n$ is the nucleon number density, $k_{F_q}=(3\pi^2\rho_q)^{1/3}$ is the Fermi momentum, and $\epsilon_{F_q}=\sqrt{k_{F_q}^2+m^{*2}}$. Here $e_{\rm ke}$, $m_e$, and $\rho_e$ are the kinetic energy density, mass, and density of electrons, respectively. Since the electron Fermi energy is much higher than the Coulomb energy, we can assume that electrons are ultrarelativistic, uniformly distributed. We can approximate $e_{\rm ke}$ to be the energy density of the uniform relativistic Fermi gas. The $e_0$ term is the usual Thomas-Fermi approach, while the $e_2$ term is the relativistic correction of the energy density of the order of $\hbar^2$.

The semiclassical ground state density $\rho_q$ and the meson and photon fields are obtained by applying the variational principle to the semiclassical energy density $e^{\rm sc}$,

$$\begin{aligned}\mu_p=&\epsilon_{F_p}+g_vV_0+eA_0-2X_{1p}\nabla^2\rho_p-X_{2p}\nabla^2m^*\\&-\frac{\partial X_{1p}}{\partial\rho_p}(\nabla\rho_p)^2-2\frac{\partial X_{1p}}{\partial m^*}(\nabla\rho_p\cdot\nabla m^*)\\&-\left(\frac{\partial X_{2p}}{\partial m^*}-\frac{\partial X_{3p}}{\partial\rho_p}\right)(\nabla m^*)^2+\frac{1}{2}g_\rho b_0,\end{aligned} \tag{14}$$

$$\begin{aligned}\mu_n=&\epsilon_{F_n}+g_vV_0-2X_{1n}\nabla^2\rho_n-X_{2n}\nabla^2m^*-\frac{\partial X_{1n}}{\partial\rho_n}(\nabla\rho_n)^2\\&-2\frac{\partial X_{1n}}{\partial m^*}(\nabla\rho_n\cdot\nabla m^*)-\left(\frac{\partial X_{2n}}{\partial m^*}-\frac{\partial X_{3n}}{\partial\rho_n}\right)(\nabla m^*)^2\\&-\frac{1}{2}g_\rho b_0,\end{aligned} \tag{15}$$

$$(\nabla^2-m_v^2)V_0=-g_v\rho, \tag{16}$$

$$(\nabla^2-m_\rho^2)b_0=-\tfrac{1}{2}g_\rho(\rho_p-\rho_n), \tag{17}$$

$$(\nabla^2-m_s^2)\phi_0=-g_s\rho_s+b\phi_0^2+c\phi_0^3, \tag{18}$$

$$\nabla^2A_0=-e(\rho_p-\rho_e), \tag{19}$$

where

$$\rho_s=\frac{\partial e^{\rm sc}}{\partial m^*} \tag{20}$$

is the semiclassical scalar density and $\mu_p$ and $\mu_n$ are the chemical potentials (including the rest mass) of protons and neutrons, respectively.

In our calculations, we assume that in the inner crusts of neutron stars, the protons are confined in nuclei and a nucleus is referred to as the space in which protons and neutrons coexist. As was done in [12], we assume that the spherical nuclei form a body-centered-cubic lattice. The whole space is divided into hexagonal cells of volume $a^3$, where $a$ is the lattice constant and each cell contains one nucleus. Although the whole space is divided into unit cells, it is still very difficult to calculate the energy of unit cells numerically. In order to simplify our calculations, the Wigner-Seitz approximation is applied. The actual hexagonal cell is replaced by the Wigner-Setiz cell which is defined as a sphere with volume $a^3$. Each cell is assumed to be electrically neutral and interactions among cells are neglected.

At a given nucleon number density $\rho$, we use Eq. (6) to calculate the total energy per unit cell. Then we minimize the average energy per nucleon with respect to variation of the proton fraction $Y_p$ ($\beta$ stability) and the lattice constant $a$. The nucleon density distributions inside the unit cell are determined by Eqs. (14)–(19). These equations constitute a set of nonlinear differential equations and are solved numerically by the imaginary time step method [19,21], which will be discussed in detail in Sec. IV. It should be noted that the solutions must satisfy the conditions of beta equilibrium and charge neutrality simultaneously. The $\beta$-stability condition requires

$$(E/N)_{(Y_p)}=\text{minimum}, \tag{21}$$

where $E/N$ is the average energy per nucleon, and this condition can be written in the familiar form [22]

$$\langle\mu_n\rangle-\langle\mu_p\rangle=\langle\mu_e\rangle, \tag{22}$$

where $\langle\mu_n\rangle$, $\langle\mu_p\rangle$, and $\langle\mu_e\rangle$ are the expectation values of chemical potentials of neutrons, protons, and electrons, respectively. Note that after neutrons drip off from nuclei, the neutron chemical potential inside nuclei is the same as that outside nuclei, and it should be independent of the position. But the proton chemical potential is independent of the position only within the nuclei. We assume that the chemical potential is the same as the Fermi energy and this is true at zero temperature. Moreover, the Fermi momentum of electrons is $k_e=(3\pi^2\rho_e)^{1/3}$ and the electron chemical potential $\mu_e$ can be written as

$$\mu_e=(k_e^2+m_e^2)^{1/2}-eA_0, \tag{23}$$

and $\mu_p$ and $\mu_n$ are obtained from Eqs. (14) and (15), respectively. The charge neutrality condition requires

$$\rho_e=\frac{\int_{\rm cell}\rho_p dr}{a^3}. \tag{24}$$

It implies that the number of protons and the number of electrons inside a unit cell are the same.

TABLE I. Parameter set BBI, BBII, and BBIII for the nonlinear BB model.

| Parameters | BBI | BBII | BBIII |
|---|---|---|---|
| $g_s$ | 8.2855 | 8.0732 | 7.8702 |
| $g_v$ | 9.2475 | 9.2475 | 9.2475 |
| $g_\rho$ | 8.8152 | 8.8152 | 8.8152 |
| $b$ (fm$^{-1}$) | 23.9076 | 15.5068 | 8.0380 |
| $c$ | −47.5412 | −12.9438 | 16.2137 |
| $m$ (MeV) | 939 | 939 | 939 |
| $m_s$ (MeV) | 500 | 500 | 500 |
| $m_v$ (MeV) | 783 | 783 | 783 |
| $m_p$ (MeV) | 763 | 763 | 763 |
| $K$ (MeV) | 200 | 250 | 300 |

## III. CHOICE OF PARAMETERS

The BB Lagrangian contains eight parameters which are the meson-nucleon coupling constants $g_v$, $g_\rho$, and $g_s$, the meson masses $m_v$, $m_\rho$, and $m_s$, and the two constants of the meson-meson self-coupling, $b$ and $c$. We choose the parameter sets taken from [23] listed in our Table I for several reasons.

First of all, these parameter sets can give reasonable saturation properties of nuclear matter. Among the saturation properties of nuclear matter, the incompressibility $K$ seems to be a main uncertainty. The experimental value of the incompressibility $K$ is obtained by the analysis of giant monopole resonance of nuclei; however, Blaizot [24] obtained $K=210\pm30$ MeV and Sharma *et al.* [25] obtained $K=300\pm25$ MeV. The corresponding nuclear matter properties such as binding energy per nucleon $E/N$, saturation density $\rho_0$, symmetry energy $a_{\rm sym}$, and effective mass $m^*/m$ at saturation are fixed at $-15.75$ MeV, 0.16 fm$^{-3}$, 36.8 MeV, and 0.75, respectively, and the range of incompressibility $K$ is from 200 to 300 MeV. We also list the incompressibility $K$ for the three parameter sets labeled BBI, BBII, and BBIII in Table I. These values are close to those obtained from the nuclear experiments. Among the parameter sets, only the BBIII set has a positive coupling constant $c$.

Second, we have used these parameter sets to calculate the binding energy, neutron rms radius, and proton rms radius of $^{40}$Ca in Table II (for detailed calculations see the next section). The results are well consistent with those of [18].

Third, following Pethick, Ravenhall, and Lorenz [26], we have compared our energy per nucleon of neutron matter as a function of density with that from the microscopic calculations [27–30] and from the Skyrme model of [31]. It can be seen from Fig. 1 that our result based on the BBIII model is very consistent with that from the Skyrme model at $\rho<0.1$ fm$^{-3}$ and is rather consistent with the microscopic ''data,'' even though our BBI and BBII results depart significantly from these ''data.''

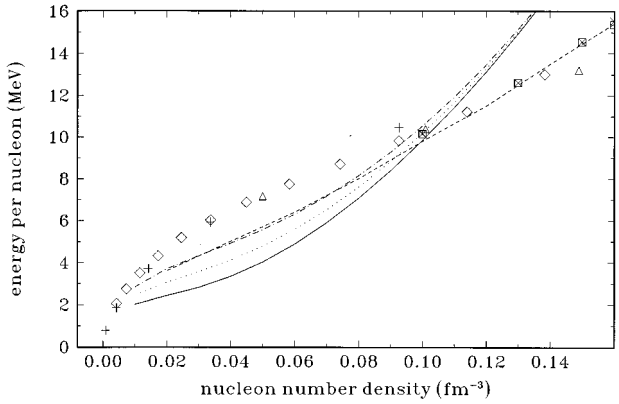


FIG. 1. Energy per nucleon of neutron matter measured from the nucleon mass as a function of nucleon number density. Results from microscopic calculations are represented with data points: The diamonds are the values obtained using the $V14$ potential plus a three-nucleon interaction from [27] and the + signs using the Reid potential from [28]. The triangles are nonrelativistic calculations using Bonn-$A$ potential from [30]. The squares and crosses are relativistic calculations using the Bonn-$A$ potential from [29] and [30]. The dashed line is taken from the Skyrme model of [31]. The solid, dotted, and dot-dash lines are our results corresponding to the BBI, BBII, and BBIII models.

Finally, we have obtained rather reasonable structures of neutron stars based on the BB models in the relativistic mean-field theory [20].

## IV. NUMERICAL SCHEME

In this section, we present the numerical method for finding the energies and density distributions of nucleons at a given density. In order to find the solutions, we have to first solve a set of coupled differential equations which consist of the field equations and the nucleon equations, then vary the proton fraction $Y_p$ to achieve the $\beta$-stability condition, and finally minimize the energy with respect to variation of the lattice constant $a$. We divide the numerical procedures into three parts as follows (a more detailed description of the numerical scheme, cf. [32]).

(1) At a given density $\rho$, a lattice constant $a$, and a proton fraction $Y_P$, the coupled equations (14)–(19) are solved numerically by the imaginary time step method [19,21], until self-consistency is achieved. The imaginary time step

TABLE II. Comparison of our calculated results with those obtained by Centelles *et al.* [18] for finite nucleus $^{40}$Ca with the parameter sets BBI, BBII, BBIII, and SRK3M7. The total binding energy is given in MeV, and the neutron rms radius and the proton rms radius are in fm.

| Parameter set | BBI | BBII | BBIII | SRK3M7 (our results) | SRK3M7 (Centelles *et al.* 1992) |
|---|---|---|---|---|---|
| $E$ (MeV) | −366.5 | −334.9 | −331.0 | −348.13 | −348.1 |
| $r_n$ (fm) | 3.14 | 3.14 | 3.14 | 3.169 | 3.17 |
| $r_p$ (fm) | 3.11 | 3.11 | 3.11 | 3.205 | 3.21 |

method has been used in nonrelativistic Hartree-Fock and extended Thomas-Fermi calculations. Consider a general time-dependent equation

$$i\frac{\partial}{\partial t}\varphi=\hat{h}\varphi, \tag{25}$$

which is formally solved as

$$\varphi(\Delta t)=\exp(-i\Delta t\hat{h})\varphi(0). \tag{26}$$

Assuming the time step $\Delta t$ is replaced by an imaginary quantity $-i\Delta\tau$, the repeated action of the exponential

$$\varphi^{(n+1)}=\exp(-\Delta\tau\hat{h})\varphi^{(n)}, \tag{27}$$

followed by a normalization of $\varphi$, causes the wave function to converge to the lowest eigenstate of $\hat{h}$.

In our case, the corresponding Euler-Lagrange equations (14) and (15),

$$\frac{\delta e^{\rm sc}}{\delta\rho_q}=\frac{\partial e^{\rm sc}}{\partial\rho_q}-\nabla\frac{\partial e^{\rm sc}}{\partial(\nabla\rho_q)}=\mu_q, \tag{28}$$

are written in a form similar to the Hartree-Fock equations

$$(-M_q\nabla^2+V_q)\psi_q=\mu_q\psi_q, \tag{29}$$

where $\psi_q=\rho_q^{1/2}$, which has no apparent physical significance. We define, for $q=$protons,

$$M_p=4X_{1p}\psi_p^2, \tag{30}$$

$$\begin{aligned}V_p&=\mu_p+M_p\frac{\nabla^2\psi_p}{\psi_p}\\&=\epsilon_{F_p}+g_vV_0+eA_0-4X_{1p}(\nabla\psi_p)^2-X_{2p}\nabla^2m^*\\&\quad-4\frac{\partial X_{1p}}{\partial\rho_p}\psi_p^2(\nabla\psi_p)^2-4\frac{\partial X_{1p}}{\partial m^*}(\psi_p\nabla\psi_p\cdot\nabla m^*)\\&\quad-\left(\frac{\partial X_{2p}}{\partial m^*}-\frac{\partial X_{3p}}{\partial\rho_p}\right)(\nabla m^*)^2+\frac{1}{2}g_\rho b_0\end{aligned} \tag{31}$$

and, for $q=$neutrons,

$$M_n=4X_{1n}\psi_n^2, \tag{32}$$

$$\begin{aligned}V_n&=\mu_n+M_n\frac{\nabla^2\psi_n}{\psi_n}\\&=\epsilon_{F_n}+g_vV_0-4X_{1n}(\nabla\psi_n)^2-X_{2n}\nabla^2m^*\\&\quad-4\frac{\partial X_{1n}}{\partial\rho_n}\psi_n^2(\nabla\psi_n)^2-4\frac{\partial X_{1n}}{\partial m^*}(\psi_n\nabla\psi_n\cdot\nabla m^*)\\&\quad-\left(\frac{\partial X_{2n}}{\partial m^*}-\frac{\partial X_{3n}}{\partial\rho_n}\right)(\nabla m^*)^2-\frac{1}{2}g_\rho b_0.\end{aligned} \tag{33}$$

For actual numerical computation, the propagation equation (27) is approximated as

$$\left(1+\frac{\Delta}{2}h_{\rm RETF}^{(n+1/2)}\right)\psi_q^{(n+1)}=\left(1-\frac{\Delta}{2}h_{\rm RETF}^{(n+1/2)}\right)\psi_q^{(n)}, \tag{34}$$

in order to avoid instabilities, and $h_{\rm RETF}^{(n+1/2)}$ is estimated between step $n$ and $n+1$ for satisfactory accuracy. We write these two equations, together with the field equations, in discretized form. The differential operators, densities, and fields are represented on a discrete mesh in coordinate space with a spacing $\Delta r\sim0.1$ fm. Between step $n$ and $n+1$, we use Gaussian elimination to solve the discrete Poisson and Helmoholtz equations to obtain the Coulomb potential $A_0$ and the Yukawa potentials $V_0$ and $b_0$, respectively. However, the scalar meson potential $\phi_0$ is particularly found by Gaussian elimination of the discrete equation

$$\begin{aligned}(\nabla^2-m_s^2)\phi_0^{(n'+1)}&=-g_s\rho_s(\rho_q^{(n)},\phi_0^{(n')})+b(\phi_0^{(n')})^2\\&\quad+c(\phi_0^{(n')})^3,\end{aligned} \tag{35}$$

where $n'$ is another index. At the $n$th-iteration stage of Eq. (34), Eq. (35) has to be iterated until consistency in $\phi_0^{(n'+1)}$ is achieved. In our calculations, $\Delta\tau$ is set to 0.004. Starting from a reasonable guess for $\rho_q$ and $\rho_s$, convergence is generally achieved to within $10^{-6}$ MeV for the energy per nucleon after about 100 iterations of Eq. (34). Note that the densities converge slower than the energy.

(2) After obtaining the solution of the second-order semiclassical variational equations, we check whether the calculated solution satisfies the $\beta$-stability condition. If not, the proton fraction $Y_p'$ is altered according to Eq. (22),

$$\langle[(3\pi^2Y_p'\rho)^{2/3}+m_e^2]^{1/2}-eA_0\rangle=\langle\mu_n\rangle-\langle\mu_p\rangle, \tag{36}$$

until the $\beta$-stability condition is satisfied. Whenever we change the proton fraction $Y_P$, the solution of the variational equations must be calculated again. It normally requires about 20 iterations of Eq. (36) to achieve the desired accuracy, $\delta Y_p\leqslant10^{-6}$.

(3) Finally, we vary the lattice constant $a$ in order to obtain the optimum energy at a given density $\rho$. Since the nucleon distributions change whenever the lattice constant $a$ is altered, the above-mentioned numerical procedures must be repeated for every value of lattice constant $a$.

For calculating the energy and nucleon density distributions of finite nuclei, only part (1) is required. To test our computer code, we compare our results for finite nuclei to those obtained in [18] with the same approach and parameter set, namely, SRK3M7. In Table II, we see that our calculated results of energies and proton and neutron rms radii for $^{40}$Ca are the same as those calculated in [18]. Figure 2 shows our results of proton density distributions of $^{40}$Ca calculated in the RETF $\hbar^2$ approximation with the parameter set SRK3M7.

In the second part of our numerical procedures, we can use Eq. (21) instead of using Eq. (22) to find the optimum proton fraction $Y_P$. Within the density range of interest, both methods yield the proton fraction that agrees to a value with discrepancies less than 0.02%.

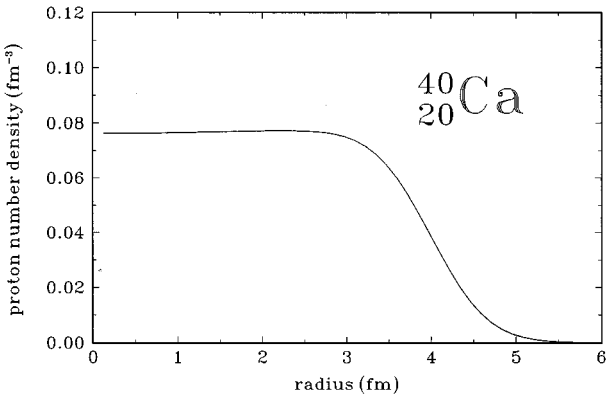


FIG. 2. Charge densities of $^{40}$Ca obtained with the parameter set SRK3M7 in the RETF $\hbar^2$ approximation.

## V. RESULTS

We can now calculate the energies of spherical nuclei and of uniform matter. By comparing the energy differences between the two phases, we can estimate the densities of the crust-core transition region and deduce the effect of incompressibility $K$. In addition, the density distributions of neutrons and protons at various densities are obtained during the calculations.

### A. Energies of spherical nuclei and uniform matter

In Table III we list the energy per nucleon (including the nucleon rest energy) of cold uniform neutron-star matter as a function of nucleon number density calculated in the BB nonlinear model with parameter sets BBI, BBII, and BBIII. One sees that the energy per nucleon of cold uniform neutron-star matter depends insensitively on the incompressibility $K$ at subnuclear densities.

We show the energy per nucleon of spherical nuclei relative to that of uniform matter in Fig. 3. For all the three parameter sets, as the density of matter increases, the differences between two phases become small, and the spherical nuclei eventually dissolve into uniform matter. The densities for transition from spherical nuclei to uniform matter are listed in Table IV. The phase transition takes place at $\rho \approx 0.058$ fm$^{-3}$ for parameter set BBI, and 0.066 and 0.073 fm$^{-3}$ for parameter sets BBII and BBIII, respectively. We can observe that the smaller the value of $K$, the lower the density at which the phase transition occurs. Although the transition densities are different for three parameter sets, the differences of $Y_p$ among various parameter sets are small. It implies that the incompressibility $K$ has little effect on the proton fraction. In Fig. 4 we show the proton fraction $Y_p$ as a function of nucleon number density with parameter set BBIII.

TABLE III. Energy per nucleon of uniform cold neutron-star matter with parameter sets BBI, BBII, and BBIII.

| Nucleon number density (fm$^{-3}$) | BBI (MeV) | BBII (MeV) | BBII (MeV) |
|---|---|---|---|
| 0.01 | 941.58407 | 941.99574 | 942.39303 |
| 0.02 | 941.96163 | 942.60384 | 943.23922 |
| 0.03 | 942.31321 | 943.06656 | 943.82504 |
| 0.04 | 942.77903 | 943.56324 | 944.36215 |
| 0.05 | 943.38934 | 944.15047 | 944.93159 |
| 0.06 | 944.14577 | 944.84844 | 945.57224 |
| 0.07 | 945.04096 | 945.66321 | 946.30462 |
| 0.08 | 946.06479 | 946.59468 | 947.13983 |
| 0.09 | 947.20676 | 947.63995 | 948.08368 |
| 0.10 | 948.45684 | 958.79488 | 949.13881 |

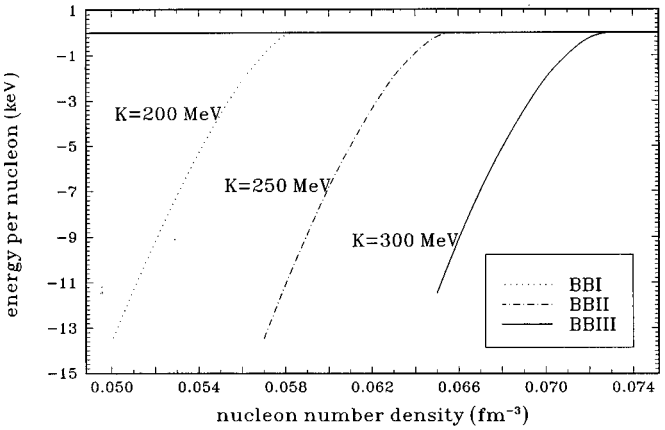


FIG. 3. Energy per nucleon of spherical nuclei relative to that of uniform matter as a function of nucleon number density.

### B. Nucleon density distributions

As the density of matter increases, all three parameter sets yield similar nucleon distributions. For illustration, we only show the results with parameter set BBIII which yields the

TABLE IV. Densities for transition from spherical nuclei to uniform matter.

| Parameter set | Transition density (fm$^{-3}$) |
|---|---|
| BBI | 0.058 |
| BBII | 0.066 |
| BBIII | 0.073 |

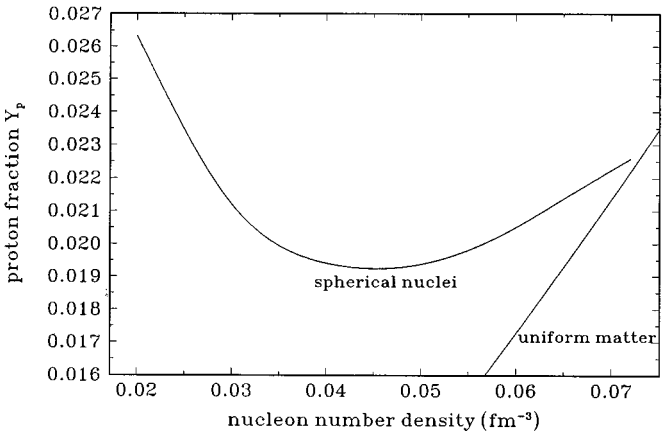


FIG. 4. Proton fraction $Y_p$ as a function of nucleon number density with parameter set BBIII ($K$=300 MeV).

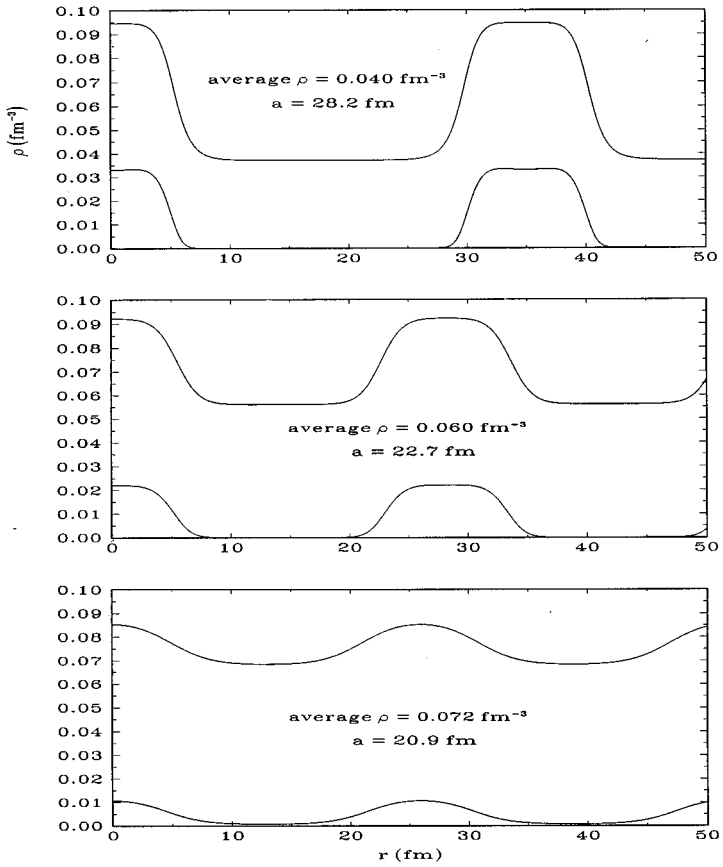


FIG. 5. Neutron (upper) and proton (lower) density distributions along an axis joining the centers of adjacent unit cells with parameter set BBIII ($K=300$ MeV).

largest phase transition density. The density distributions of neutrons and protons at different nucleon number densities are presented in Fig. 5, which shows the densities along an axis joining the centers of adjacent unit cells. It can be observed that the lattice constant $a$ reduces and the nuclear density distributions become more and more uniform as the matter density increases. The obtained results are consistent with those obtained in [1]. It can be seen from Fig. 5 that the assumption of a sharp nuclear surface used in the compressible liquid drop calculations is unrealistic.

### C. Energy of nonspherical nuclei

We now consider the nonspherical nuclei in this subsection. As was done in [12], the stable nonspherical nuclear shapes we consider are cylinder and slab. We assume that cylinder nuclei form a two-dimensional hexagonal lattice. Similar to the case of spherical nuclei, we divide the whole space into appropriate unit cells of volume $a^3$. The unit cell for cylinder nuclei is a prism with base area $a^2$ and height $a$. For slab nuclei, the unit cell is a cube whose edge is equal to the lattice constant $a$. To simplify the calculation, we also use the Wigner-Seitz unit cell of a cylinder with base area $a^2$ and height $a$ to replace the actual unit cell of a prism for cylindrical nuclei. The energy differences between various shapes of nuclei and uniform matter are shown in Fig. 6. We find that the energetically most favorable nuclear shape changes directly from spherical to uniform matter for all three parameter sets. That means the phases with nonspherical nuclei are never in the equilibrium state at any density in our models.

## VI. DISCUSSION AND CONCLUSIONS

In the past there have been many studies of the nuclei in neutron-star crusts and the transition to the uniform phase (for a brief review see [26]). The earliest works [4,5] were based on the use of a semiempirical formula to estimate the masses of the nuclei, together with an expression for the energy of the neutron gas outside nuclei calculated from many-body theory and the nucleon-nucleon interaction. These led to rather low densities for the transition between the nuclear phase and the uniform one. In the case of [4], the density was about $0.3\rho_0 \sim 5\times10^{13}$ g cm$^{-3}$, while the work of [5] gave a slightly small density. In both of these works the transition was found to be relatively sharp. The important point of the works in [6–8] is that the energy of nuclear matter in nuclei and the energy of the neutron matter outside were evaluated from one and the same expression for the energy density as a function of neutron and proton densities. The transition density given in [6] was close to the saturation density of symmetric nuclear matter, while in the latter two references it was about $1.5\times10^{14}$ g cm$^{-3}$, or just over half the saturation density. The most recent development is the discovery [12,13] that in a large fraction of the crustal matter, nuclei may be rodlike or platelike rather than of roughly spherical shape. Oyamatsu [12] used the Thomas-Fermi calculations with four energy density functionals and found that the transition densities were between 0.086 and 0.094 fm$^{-3}$. Lorenz *et al.* [13] adopted two microscopic interactions named the Skyrme interaction and the interaction of [27] and

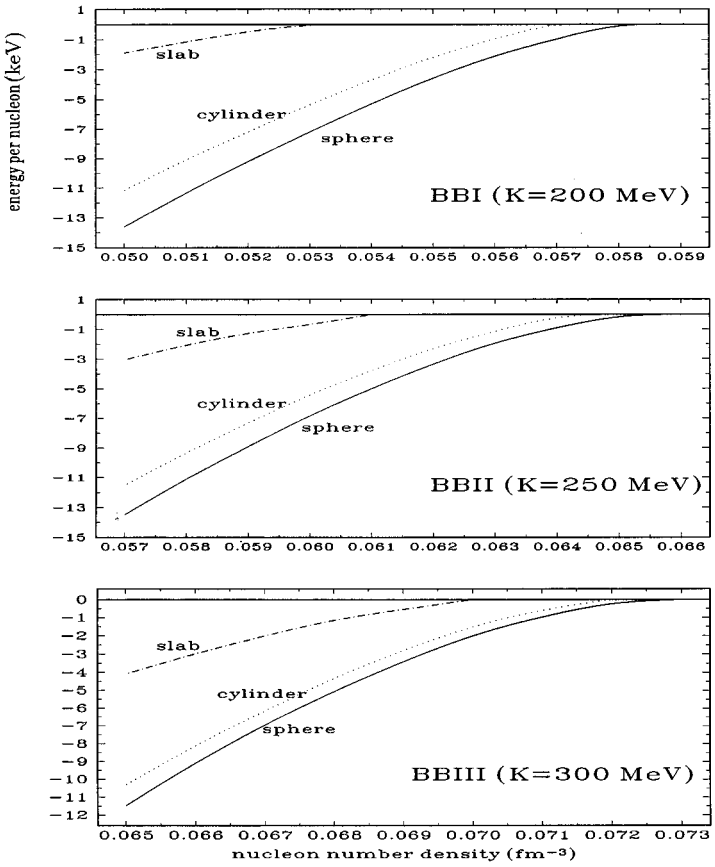


FIG. 6. Energy differences between various shapes of nuclei and uniform matter.

obtained transition densities of about 0.0725 and 0.0957 $\mathrm{fm}^{-3}$, respectively.

In this paper, the properties of nuclei, i.e., energies, shapes, and nucleon density distributions, in the inner crusts of neutron stars are studied in the framework of a relativistic mean field (RMF). We perform the semiclassical relativistic extended Thomas-Fermi (RETF) calculations for the relativistic nonlinear ($\sigma$, $\omega$, $\rho$) model with three sets of parameters, which cover the commonly accepted range for the incompressibility $K$ (see Table I). The parameters of the effective Lagrangian are fitted to the bulk properties of nuclear matter except that the incompressibility $K$ is treated as an unknown. We find that the density of the crust-core transition region increases with an increase of the incompressibility $K$ and the largest phase transition density to uniform matter found is $\rho \approx 0.073$ $\mathrm{fm}^{-3}$, a density well below the nuclear density $\rho_0$. If a neutron star has a lower phase transition density, its mass and moment of inertia of the crust will be reduced. Since these two quantities play important roles in models of glitches (e.g., see [33]) and of thermal evolution (e.g., [34–36]), it is expected that with astronomical observations such as surface radiation and glitch events of neutron stars, our calculated results can be indirectly tested.

We also find that spherical nuclei are the only equilibrium state in the inner crust of neutron stars. It can be seen that our results are not in good agreement with the Thomas-Fermi calculations of Oyamatsu [12]. His study gives that the nuclear shape changes from sphere to cylinder, slab, cylindrical hole, and spherical hole successively as the density increases and obtains higher phase transition density. However, it is very interesting that our results are very similar to the recent results obtained in [13] based on the SKM interaction. In these liquid drop calculations, two different Skyrme-type interactions named FPS and SKM are used. The two interactions yield two different results, and the results for the FPS interaction are similar to that of [12]. Therefore the calculated results are sensitively dependent on the still incompletely understood nucleon-nucleon interaction.

We next analyze why the phase containing spherical nuclei is favored in the present case over the phase containing nonspherical nuclei in the inner crust of a neutron star. Following Ref. [3], the density range in which the latter phase may appear can be delimited by some general considerations. At the lower end, the appearance of nonspherical nuclei may be due to the instability of spherical nuclei to fission. At the upper end, there is a limiting density at which the phase transition from nuclei to uniform nuclear matter occurs. The Bohr-Wheeler condition for the fission of isolated spherical nuclei is that the nuclear Coulomb energy $E_{\mathrm{Coul}} \geqslant 2E_{\mathrm{surf}}$ (where $E_{\mathrm{surf}}$ is the surface energy). Furthermore, the condition for equilibrium under strong interactions in the crust of a neutron star requires $E_{\mathrm{surf}} = 2E_{\mathrm{Coul}}(1-1.5r_N/r_{\mathrm{cell}})$, where $r_N$ and $r_{\mathrm{cell}}$ are the nuclear radius and the Wigner-Seitz cell radius, respectively. These two conditions show that if $r_N/r_{\mathrm{cell}} \geqslant 1/2$, the equilibrium nuclei are unstable to fission. This corresponds to nuclei filling 1/8 of space. In the deep layers of the inner crust of a neutron star, the dripped-neutron density is usually $\sim 50\%$ of the nuclear density $n_i$ [3]. So as the matter density increases to $\sim 5n_i/9$, spherical

nuclei are unstable to fission. In the present case, $n_i \approx 0.15$ fm$^{-3}$ and thus the lower limiting density for the appearance of nonspherical nuclei, $n_{\rm low} \sim 0.083$ fm$^{-3}$. Because the density for the phase transition from nuclei to uniform nuclear matter (see Table IV) is less than $n_{\rm low}$, we conclude that the spherical nuclei may be only the equilibrium state in our case. From Table 3 in [3], we can see that for the Skyrme interaction or the interaction of [27] the density for the appearance of nonspherical nuclei is less than that for the transition from the phase containing nuclei to uniform nuclear matter. Thus, for these interactions nonspherical nuclei can reasonably exist in the inner crust of a neutron star.

It is possible that improvements of our work can be made in future studies. For example, shell effects of different nuclear shapes may be included. By using the so-called expectation value method, Centelles *et al.* [18] incorporated shell effects into the semiclassical calculation for spherical finite nuclei. Besides, we may calculate the Coulomb energy accurately rather than use the Wigner-Seitz approximation to simplify our calculations. It has been shown that the difference between the exact value and the results of the Wigner-Seitz approximation is dependent on the nuclear shapes [11].

K.S.C. and C.C.Y. thank the UPGC of Hong Kong for support; Z.G.D. thanks the National Natural Science Foundation of China for support.

[1] J. W. Negele and D. Vautherin, Nucl. Phys. **A207**, 298 (1973).
[2] C. J. Pethick and D. G. Ravenhall, in *The Lives of the Neutron Stars*, edited by M. A. Alpar, Ü. Kilziloğlu, and J. van Paradijs (Kluwer Academic Publishers, Dordrecht, 1995).
[3] C. J. Pethick and D. G. Ravenhall, Annu. Rev. Nucl. Part. Sci. **45**, 429 (1995).
[4] W. D. Langer, L. C. Rosen, J. M. Cohen, and A. G. W. Cameron, Astrophys. Space Sci. **5**, 529 (1969).
[5] H. A. Bethe, G. Börner, and K. Sato, Astron. Astrophys. **7**, 270 (1970).
[6] G. Baym, H. A. Bethe, and C. J. Pethick, Nucl. Phys. **A175**, 225 (1971).
[7] J. Arponen, Nucl. Phys. **A191**, 257 (1972).
[8] J. R. Buchler and Z. Barkat, Phys. Rev. Lett. **27**, 48 (1971).
[9] D. G. Ravenhall, C. J. Pethick, and J. R. Wilson, Phys. Rev. Lett. **50**, 2066 (1983).
[10] M. Hashimoto, H. Seki, and M. Yamada, Prog. Theor. Phys. **72**, 373 (1984).
[11] K. Oyamatsu, M. Hashimoto, and M. Yamada, Prog. Theor. Phys. **71**, 320 (1984).
[12] K. Oyamatsu, Nucl. Phys. **A561**, 431 (1993).
[13] C. P. Lorenz, D. G. Ravenhall, and C. J. Pethick, Phys. Rev. Lett. **70**, 379 (1993).
[14] F. V. De Blasio and G. Lazzari, Phys. Rev. C **52**, 418 (1995).
[15] P. G. Reinhard, Rep. Prog. Phys. **52**, 439 (1989).
[16] J. D. Walecka, Ann. Phys. (N.Y.) **83**, 491 (1974).
[17] J. Boguta and A. R. Bodmer, Nucl. Phys. **A292**, 413 (1977).
[18] M. Centelles, X. Viñas, M. Barranco, S. Marcos, and R. J. Lombard, Nucl. Phys. **A537**, 486 (1992).
[19] M. Centelles, X. Viñas, M. Barranco, and P. Schuck, Ann. Phys. (N.Y.) **221**, 165 (1993).
[20] K. S. Cheng, Z. G. Dai, and C. C. Yao, Astrophys. J. **464**, 348 (1996).
[21] J. A. Maruhn and S. E. Koonin, *Computational Nuclear Physics* (Springer-Verlag, Berlin, 1993), p. 115.
[22] S. L. Shapiro and S. A. Teukolsky, *Black Holes, White Dwarfs, and Neutron Stars: The Physics of Compact Objects* (Wiley, New York, 1983), p. 230.
[23] D. Von-Eiff, W. Stocker, and M. K. Weigel, Phys. Rev. C **50**, 1436 (1994).
[24] J. P. Blaizot, Phys. Rep. **64**, 171 (1980).
[25] M. M. Sharma, W. T. A. Borghols, S. Brandenburg, S. Crona, A. van der Woude, and M. N. Harakeh, Phys. Rev. C **38**, 2562 (1988).
[26] C. J. Pethick, D. G. Ravenhall, and C. P. Lorenz, Nucl. Phys. **A584**, 675 (1995).
[27] B. Friedman and V. R. Pandharipande, Nucl. Phys. **A361**, 502 (1981).
[28] P. J. Siemans and V. R. Pandharipande, Nucl. Phys. **A173**, 561 (1971).
[29] D. G. Li, R. Machleidt, and R. Brockmann, Phys. Rev. C **45**, 2782 (1992).
[30] G. Bao, L. Engvik, M. Hjorth-Jensen, E. Osnes, and E. Ostgaard, Nucl. Phys. **A575**, 707 (1994).
[31] J. Skalski, P. Heenen, and P. Bonche, Nucl. Phys. **A559**, 221 (1993).
[32] C. C. Yao, Masters thesis, University of Hong Kong, 1996.
[33] M. A. Alpar, H. F. Chau, K. S. Cheng, and D. Pines, Astrophys. J. **409**, 345 (1993).
[34] S. Tsuruta, in *The Lives of the Neutron Stars* [2].
[35] N. Chong and K. S. Cheng, Astrophys. J. **409**, 219 (1993).
[36] N. Chong and K. S. Cheng, Astrophys. J. **425**, 210 (1994).